

RESEARCH ARTICLE | SEPTEMBER 23 2024

# Bayesian-inverted laser Thomson scattering measurements indicate electrostatic erosion pathways in magnetically-shielded Hall effect thrusters <sup>EP</sup>

Jean Luis Suazo Betancourt ; Julian Lopez-Uricoechea ; Naia Butler-Craig ; Adam M. Steinberg ; Mitchell L. R. Walker

Check for updates

*J. Appl. Phys.* 136, 123301 (2024)  
<https://doi.org/10.1063/5.0221547>



Nanotechnology & Materials Science


Optics & Photonics

Impedance Analysis

Scanning Probe Microscopy


Sensors

Failure Analysis & Semiconductors



**Unlock the Full Spectrum.**  
From DC to 8.5 GHz.  
Your Application. Measured.

[Find out more](#)



# Bayesian-inverted laser Thomson scattering measurements indicate electrostatic erosion pathways in magnetically-shielded Hall effect thrusters

Cite as: J. Appl. Phys. **136**, 123301 (2024); doi: [10.1063/5.0221547](https://doi.org/10.1063/5.0221547)

Submitted: 1 June 2024 · Accepted: 9 September 2024 ·

Published Online: 23 September 2024



View Online



Export Citation



CrossMark

Jean Luis Suazo Betancourt,<sup>a)</sup>  Julian Lopez-Uricoechea,  Naia Butler-Craig,  Adam M. Steinberg,   
and Mitchell L. R. Walker 

## AFFILIATIONS

School of Aerospace Engineering, Georgia Institute of Technology, Atlanta, Georgia 30318, USA

<sup>a)</sup>Author to whom correspondence should be addressed: [jlsb3@gatech.edu](mailto:jlsb3@gatech.edu)

## ABSTRACT

Magnetically shielded Hall effect thrusters suffer from pole erosion as their life-limiting mechanism. However, the dominant physical mechanism causing this erosion remains unclear, limiting the ability to create designs that mitigate erosion and the predictive accuracy of simulations used to aid in design. This paper provides spatially resolved laser Thomson scattering measurements of electron temperature and density in the near field plume of a magnetically shielded Hall effect thruster, traversing the front pole region from the discharge channel centerline to the cathode centerline. The signals are inverted in a Bayesian framework, and the data are compared qualitatively and quantitatively to simulations of the same Hall effect thruster. Based on the electron momentum equation, electron pressure gradient is used as a proxy for the electron-predicted electrostatic potential gradient. To within the accuracy of this approximation, the electron pressure has a minimum immediately in front of the front pole. Hence, ions have an electrostatic potential avenue from the discharge region to the front pole, validating this mechanism of pole erosion.

© 2024 Author(s). All article content, except where otherwise noted, is licensed under a Creative Commons Attribution (CC BY) license (<https://creativecommons.org/licenses/by/4.0/>). <https://doi.org/10.1063/5.0221547>

## I. INTRODUCTION

Hall effect thrusters (HETs) are electrostatic devices that create thrust through the acceleration of ions produced by neutral propellant ionization with magnetized electrons from a hollow cathode electron source.<sup>1–4</sup> They are conventionally cylindrical in shape with a single discharge channel, although non-conventional architectures have been studied<sup>5–7</sup> and are reviewed in Chhavi and Walker.<sup>8</sup> Modern stationary plasma thruster type HETs with non-conducting discharge channel walls can be unshielded (US) or magnetically shielded (MS). The main difference between US and MS thrusters lies in their magnetic field topology and channel wall chamfering. Thrusters having notionally US and MS configurations are shown in Fig. 1.

The allure of HETs for space missions stems from their mass utilization efficiency. However, US HETs suffer from channel erosion as their life-limiting factor. The high electron temperature

of the plasma close to the wall, and deviation from equipotentialization parallel to the channel walls, accelerate ions toward the channel and then through the near-wall sheath potential.<sup>9,10</sup> The erosion of the channel walls in US HETs exposes the interior of the HETs to the plasma, destroying the magnetic circuit and effecting the electrical isolation, both of which are critical for operation especially in non-thruster-floating electrical boundary configurations.<sup>11,12</sup> This effectively limits the useful life of US thrusters to about 10,000 hours. Magnetic shielding, described below, reduces these channel erosion rates by 2–3 orders of magnitude.<sup>13–15</sup> This would suggest lifetimes exceeding 1 million hours. However, front magnetic pole erosion rates limit this to about 50 khrs at 6 kW discharge operating power with a 3.5 mm thick graphite pole cover to shield this region from direct wear.<sup>16</sup> Lifetimes exceeding 25 khrs are required for deeper space applications.

25 September 2024, 16:36:34

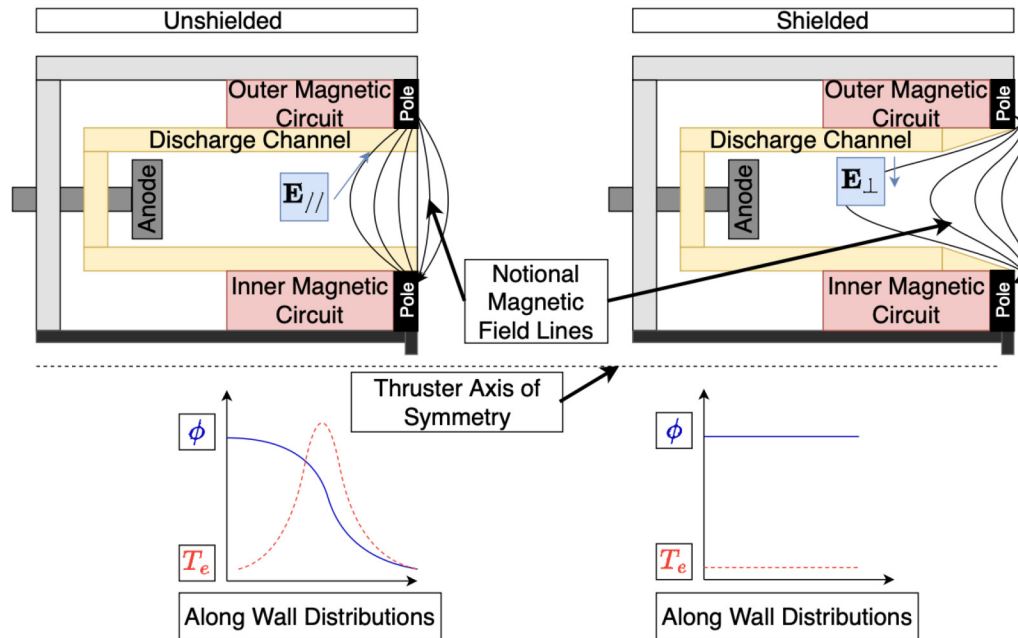


FIG. 1. Notional effect of magnetically shielding the channel walls.

In MS HETs, the design of magnetic field lines near the walls preserves equipotentialization and extends the near-wall lines close to the anode.<sup>15,17</sup> This is different from other attempts at leveraging magnetic fields to shield the channel walls, including magnetic mirrors.<sup>18</sup> The MS HET theory presented in Mikellides *et al.*<sup>15</sup> was validated in a companion paper that detailed the experiments on a retrofit of an unshielded H6 thruster into the H6MS, a magnetically shielded H6 variant.<sup>19</sup> The wall grazing magnetic field lines, which extend into the anode region with low electron temperatures, keep the electron temperature along the wall low and the potential high (similar to the discharge potential), leading to an almost fully perpendicular electric field near the wall. Given that the grazing field line is parallel to the wall, the electric field shields the wall from high-energy ions. This is shown notionally via the near-wall potential and temperature distributions in Fig. 1.

MS HETs effectively shield the channel walls from ion bombardment, reducing the rate of channel erosion and effectively eliminating channel erosion as the life-limiting factor for MS HETs. However, this leads other phenomena that occur at much slower rates, such as pole erosion, to emerge as the primary life-limiting concern. Pole erosion is the wear of the front-facing inner pole region due to ion bombardment. Pole erosion was first observed after unexpected sputtering of the magnetic pole during wear tests of the H6MS.<sup>20</sup> Investigations have shown that the largest surface topography changes occur at the point where the field lines terminate near the front magnetic pole, as measured by electrostatic probes.<sup>21</sup>

However, it remains unknown whether the underlying mechanism is due to electrostatic potentials that can accelerate ions to the

pole from the discharge region or near-pole plasma heating due to plasma instabilities. Laser induced fluorescence (LIF), surface-mounted probes, and translating probes confirmed the acceleration of ions toward the pole.<sup>16</sup> The ion flux was found to originate in the vicinity immediately adjacent to the pole, being comprised of low-velocity ions that were not accelerated with the bulk of the beam ions, validating predictions made in Mikellides *et al.*<sup>22</sup> However, additional LIF measurements and comparisons with numerical simulations in Ortega *et al.*<sup>23</sup> confirmed that plasma conditions in the near pole region can excite instabilities in the lower hybrid frequency range. An idealized model developed to scale the ion velocity distribution function with the lower hybrid frequency brought erosion rates at the inner pole close to wear test measurements, indicating that instabilities may play a role in the erosion of the front pole.

It was speculated, but not confirmed, by Jorns *et al.*<sup>16</sup> that a lower population of higher energy ions was also accelerated toward the pole with high kinetic energy due to shifts in the acceleration region caused by magnetic shielding. A 2D plasma simulation predicted that plasma potential contours at the channel edge can accelerate high-energy ions from the edge of the acceleration region to the pole surface.<sup>24</sup> It was also predicted that pole erosion is not unique to MS thrusters but a phenomenon in all HETs. However, larger potentials due to magnetic shielding at the thruster exit plane as a result of the movement of the acceleration zone are predicted to exacerbate the pole erosion in MS HETs.<sup>25</sup>

In order to optimally design HETs and predict their service life, accurate simulations are needed. The physics of HET operation are described by highly nonlinear coupled partial differential

equations.<sup>26,27</sup> HET simulations are built on many physics-based closure models. Unknown terms in models are confined and tuned/calibrated through measurements to be accurate in certain parts of the thruster over a given operational regime; oftentimes, models that help to close the governing equations have scalings that depend on critical plasma parameters such as the local magnetic flux density, electron temperature, and density. Therefore, validating and calibrating these simulations, especially in the near-field plume and pole region of an MS HET, is very challenging. For example, spatial variations in quantities that would validate or invalidate certain models occur over small length scales that are difficult to resolve using electrostatic probes without perturbing the plasma, particularly in the harsh environment  $\mathcal{O}(10\text{ mm})$  downstream of thruster discharge channel exit.<sup>28,29</sup>

Accurate validation and calibration of predictive MS HET simulations require minimally invasive investigations in the near-field plume. To date, erosion of the inner front-facing magnetic pole region of MS HETs has been observed, but simulations that self-consistently reproduce isothermal magnetic field lines fail to predict accurate erosion rates without calibration.<sup>24,30</sup> These simulations adjust profiles of unknown terms in closure models, like the anomalous electron transport across magnetic field lines, until key results like discharge channel centerline plasma property profiles agree with measured profiles.<sup>31</sup>

Incoherent laser Thomson scattering (LTS) is a minimally invasive diagnostic that can be used in the harsh near-plume plasma environment and provide direct measurements of electron thermal properties. Recently, LTS was used to study axial variation in electron properties and electron Mach number in hollow cathodes, as well as heat flux and electron diffusion in the plume of a high power HET.<sup>32–35</sup> Within the field of space electric propulsion, these studies solidify LTS as a reliable measurement tool for investigations in live HET test articles, despite the challenges associated with pushing toward the lower density detection limits in the discharge and pole region of HETs.

The primary objective of this work is to experimentally assess whether the electron temperature and density fields in the near field of a MS HET predict an avenue for ions to travel from an MS HET discharge region to the front pole. This is achieved through spatially-resolved electron property measurements made using incoherent LTS. The resultant data are also invaluable for advancement and validation of simulations of the studied thruster.

This paper is structured as follows. Section II briefly describes the experimental setup of the LTS diagnostic, the test article and discharge condition, and then briefly describes the scattering theory, off-centerline stray light collection, and signal inversion procedures. Then, Sec. III presents and discusses the electron temperature and density profiles along the discharge channel and cathode centerlines as well as traversing the front pole region. Finally, conclusions and impact of the measurements are presented in Sec. IV.

## II. EXPERIMENTAL SETUP AND ANALYSIS OF SCATTERING SIGNALS

### A. Vacuum test facility

This experiment was conducted in Vacuum Test Facility 2 (VTF-2) at the Georgia Tech High Power Electric Propulsion

Laboratory (HPEPL). VTF-2 is a 4.9 m diameter and 9.2 m long stainless-steel chamber. The operation of VTF-2 is described in Kieckhafer and Walker.<sup>36</sup>

Accurate knowledge of the chamber pressure during pump-down is important for calibration of the LTS measurements via laser Raman scattering (LRS, see below). From the atmospheric pressure of ca. 760 Torr to a medium vacuum of 1 Torr, the pressure in the facility was measured using a Kurt J Lesker XCG-BT-FB-1 capacitance manometer mounted on a flange at the periphery of the chamber. The error in the calibrated manometer pressure output vs the expected local atmospheric pressure due to the horizontal mounting of the manometer was corrected using a linear fit. The medium vacuum pressure to 1 mTorr was measured using an MKS Baratron 626B.1TCE capacitance manometer that was also mounted on the periphery of the chamber. Capacitance manometers were chosen for their accuracy of  $\pm 0.5\%$  and the fact that no gas-specific corrections are needed.

At high vacuum, the pressure at 0.5 m radially from the test section and at the periphery of the facility mounted to a flange were measured via two Agilent Bayard-Alpert 571 hot-filament ionization gauges. The operational pressures during the experiments presented are the average of the two internal and external pressures ( $p_{\text{operational}}$ ), corrected ( $p_{\text{operational}} - p_{\text{corrected}}$ ) to krypton through a linear relationship with the base pressure ( $p_{\text{base}}$ ), through

$$p_{\text{operational}} - p_{\text{corrected}} = \frac{1}{c_{\text{corr}}} (p_{\text{operational}} - p_{\text{base}}) + p_{\text{base}}, \quad (1)$$

with  $c_{\text{corr}} = 1.96$  for krypton.<sup>37</sup> This paper outlines separate experiments conducted over several days. The corrected operational pressures for each experiment are presented in their respective subsections since they vary between experiments.

Mass flow was provided by two MKS GE40A mass flow controllers mounted externally to the facility. The mass flow controllers were calibrated in the test section of VTF-2 using a DryCal 800-10 volumetric flow rate meter system.

### B. Thruster discharge and relative motion

The test article in this experiment was the H9,<sup>38</sup> shown in Fig. 2, a 9 kW class MS HET referred to henceforth as “the thruster.” The thruster is designed to operate with an internal and coaxial 60 A class lanthanum hexaboride ( $\text{LaB}_6$ ) hollow cathode, whose design heritage stems from the HERMeS and H6 HETs hollow cathodes.<sup>39</sup> The H9 cathode is henceforth referred to as “the cathode.” The operational envelopes of the H9 at standard current densities on xenon and krypton are outlined in Refs. 38, 40, 41, and 42. The operation of the H9 at high and ultra-high current densities is outlined in Refs. 43 and 44.

Note that the thruster coordinates used in this work ( $z, r$ ) have their origin at the thruster centerline and discharge channel exit plane; these coordinates generally are normalized by the thruster outer radius  $r_0$ . The vacuum chamber and light collection coordinates are as indicated in Fig. 2. As described in Sec. II C, LTS provides point-wise measurement of the electron properties at a fixed location in space that is set by the laser beam focus, with the focused beam having an estimated  $100\mu\text{m}$  beam diameter. In order to spatially

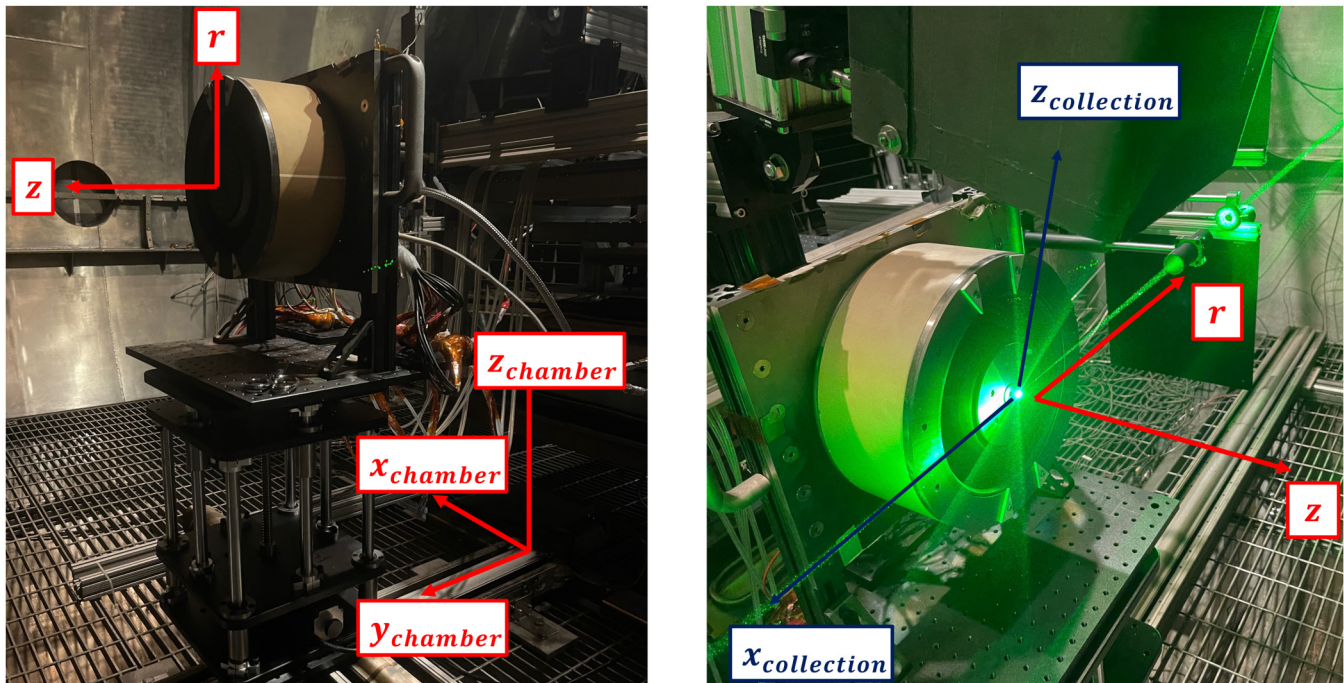


FIG. 2. Annotated picture with all of the relevant basis vectors.

resolve the electron properties in the near-field thruster plume, the thruster was mounted on planar motion stages that allowed for three-axis movement relative to the laser beam, with a maximum positional uncertainty of  $150\ \mu\text{m}$ . The interrogation points were spaced by at least 1 mm axially and 2 mm radially, exceeding the estimated  $1.4\ \text{mm} \times 100\ \mu\text{m}$  interrogation volume size in either direction. Vibrations from the chamber and other equipment did not play a major role in positional uncertainty, however, the compression of the chamber relative to the external portions of the optical system impacted the system alignment, please see Suazo Betancourt *et al.*<sup>34,45</sup> for details on the test performed to determine this.

The discharge condition for this experiment was taken to be 6 kW at a voltage of 150 V and a current of 40 A, well within the high current density regime.<sup>43</sup> Note that this condition is different than the nominal 6 kW, 300 V, 20 A condition often studied in this thruster. However, the latter condition did not produce a sufficiently high electron number density for accurate measurement. In transitioning from the nominal 6 kW, 20 A condition to the high current density 6 kW, 40 A condition, the magnet circuit currents were adjusted while keeping the inner and outer coil current ratio constant to minimize discharge oscillations and maintain the field topology, as per recommendations in Su and Jorns.<sup>40</sup> The coil current ratio did not vary, and the absolute value of the coil currents were determined to be optimal at the same values as that of the nominal 6 kW case in our high current density case.

The magnetic field topology is expected to be the same as the originally quantified magnetic field topology across all H9 thrusters

when the inner and outer coil current ratio is held constant.<sup>38,46</sup> In general, the flux density can vary with different operating conditions and propellant, as is noted in.<sup>40</sup> In general, the flux density is tuned to optimize for thruster stability by varying the absolute inner coil current value while holding constant the coil current ratio.<sup>40</sup> With this guidance, the optimal thruster stability flux density during our experiment could be compared to the work in Su *et al.*<sup>40</sup> to ensure that our value was reasonable. On krypton, the value of the flux density is expected to be 87.5% of that on xenon at the normal current density 6 kW condition. Our stability-optimized flux density based on the absolute value of the inner coil current was the same as the normal current density condition. Additionally, measurement of the magnetic flux density at  $z/r_0 = 0.013$  along the channel centerline at our optimal inner coil current value indicated a difference of less than 1% with respect to the expected value at that location. Therefore, the magnetic field topology, which is dictated by the current ratio, and the maximum flux density relative to the nominal condition on xenon, which is indicated by the point-measured maximum magnetic flux density, are consistent with expectations and previous measurements. Additionally, simulations and measurements shared by collaborators at JPL showed that the magnetic field topology simulations and measurements differed by no more than 2% at the inner discharge channel walls, and were almost perfectly aligned in the near field plume region outside of the discharge channel.<sup>46</sup> Hence, the magnetic field topology at these conditions is expected to be consistent with previous measurements.

The thruster discharge circuit was floating for all experiments. The cathode keeper, cathode heater, and thruster inner and outer magnetic circuits were operated using TDK-Lambda GEN60-25, GEN600-2.6, GEN80-42, and GEN40-38 power supplies, respectively. This series of power supplies was chosen due to their rated voltage and current accuracies of 1% of the desired outputs. The thruster discharge power supply was a Magna-Power Electronics TSA800-54, chosen for its voltage and current output accuracies of  $\pm 0.075\%$  of full scale. All power supplies were calibrated using a Fluke 83V multimeter. The maximum voltage and current divergence between the power supply displays and the multimeter was less than 1%. The thruster discharge supply was isolated from the thruster using a low-pass discharge filter described by Martinez *et al.*<sup>47</sup> The thruster-side of the discharge filter was probed using a Teledyne Lecroy HDO6104 oscilloscope to capture the dynamics of the thruster discharge voltage and current. The discharge current was probed using a Teledyne Lecroy CP150 model current clamp, and the discharge and cathode-to-ground voltages were measured using Powertek DP-25 differential voltage probes.

### C. Interrogation, collection, and detection optical systems

The collection and detection systems were thoroughly described in Suazo Betancourt *et al.*;<sup>34</sup> only a brief overview is provided here, highlighting minor changes from the previous work. The overall optical layout is shown in Fig. 3.

An injection-seeded, frequency-doubled Amplitude DLS Powerlite 9010 Nd:YAG laser (9 mm diameter, pulse duration between 5 and 8 ns, 1 J/pulse at 532 nm) was used to stimulate the Thomson and Raman scattering. The laser beam was steered, externally to the vacuum chamber, along three legs that bring the beam to coincide with  $\mathbf{x}_{\text{chamber}}$ . In addition to positioning the laser beam, these optics also oriented the polarization correctly relative to the scattering collection optical axis, focused the beam, and controlled the incident laser energy into the facility. For these experiments, the beam was expanded in a 1.5:1 configuration and a 600 mm final focusing lens was used, as opposed to the 2:1 expansion and 400 mm focusing lens in previous work.<sup>34</sup> This allowed an increase in laser pulse energy to 1.0 J/pulse without laser-induced ionization of neutrals, thus improving the signal-to-noise ratio.

The light collection and detection system was designed to maximize the collection solid angle, provide a spatial resolution of less than  $2 \times 2 \text{ mm}^2$ , and facilitate realignment of the collection and interrogation optical axes when misalignment occurred due to facility shifts. Two FG200LEA-FBUNDLE custom fiber bundles were used in the collection system. The bundles were a linear array of seven  $200 \mu\text{m}$  FG200LEA multimode fibers. The collection lenses and the glass window protecting them were the same as those in the previous implementation. The collection optics were placed in a box for protection from the plasma environment in the vacuum chamber, which was expected to be harsher than the previous stand-alone cathode experiments.<sup>34</sup>

The angle of the collection axis with respect to the face of the thruster face was approximately  $17^\circ$ . This allowed the collection volume to be positioned less than 1 mm from the thruster exit plane without the thruster hardware blocking the solid angle

subtended by the collection optics. Note that the collection angle and direction of the scattering wave vector determine the component of the electron properties that are measured; in the current configuration, this component is not aligned with the thruster basis vectors. Reported electron temperatures are along the scattering wave vector. The temperature component is  $17^\circ$  forward with respect to the face of the thruster and  $45^\circ$  clockwise.

The spectrograph was comprised of a Princeton Instruments ISOPLANE-320A spectrometer and PM4-1024i-HB-FG-18-P46 PIMAX4 ICCD camera. The spectrometer was operated with a ARC-SP-ES motorized slit, a SLIT SHUTTER-ISOPLANE320 slit shutter, and a 500 nm optimized I3-120-500-P 1200 l/mm grating. A four-lens relay system was used to capture all of the light from the fiber, relay it without clipping, and focus it into the spectrometer. The optical focal lengths were selected using ray-matrix optics in order to respect the Helmholtz optical invariant. This required a magnification of approximately 2.02. The system used two 25 mm aperture volume Bragg grating notch filters from OptiGrate, recovering most of the collection power that was lost in previous work due to clipping on 15 mm aperture filters.<sup>34</sup> A Berkeley Nucleonics BNC-577-8C model delay generator was used as the master clock for the synchronization of timing events in the system.

Alignment of the system, and hence the overall optical efficiency, was not affected by vibrations from the mechanical pump, blower, and compressors driving the radiation shrouds. While the system alignment had to be maintained and adjusted during the pump-down of the vacuum chamber, this was achieved by minor adjustment of the collection fiber optic position.<sup>34</sup> Additionally, the high laser power used in these experiments and the lack of convective cooling in the vacuum chamber made the system alignment sensitive to variations in the temperature of some optical elements. This issue is discussed further in Sec. III A.

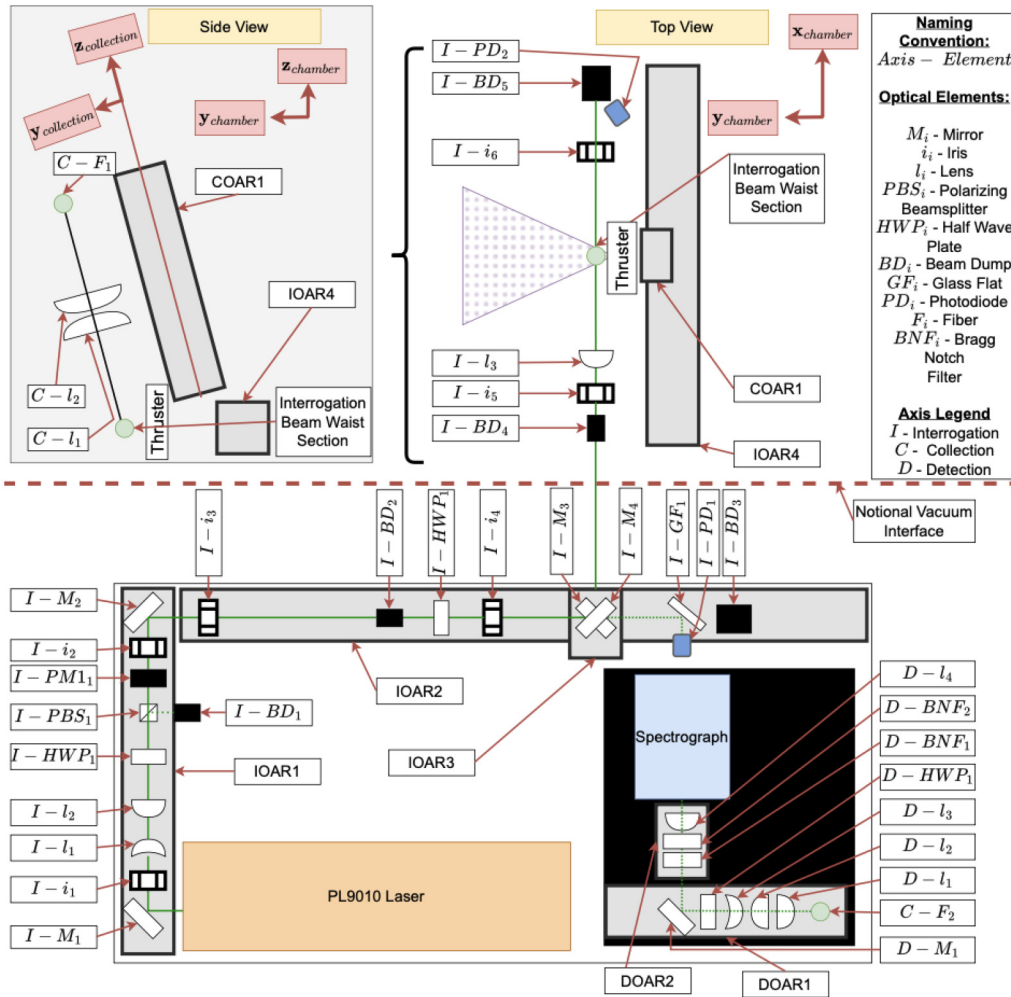
### D. Theory and analysis of scattering signals

Laser rotational Raman scattering is necessary in order to calibrate the absolute electron number density measurements in an LTS experiment. LRS is the inelastic scattering of incident radiation from polyatomic molecules as the result of a net exchange of energy from the incident radiation and the internal energy modes of the molecule.<sup>48,49</sup> The quantities of interest (QoI) in our calibration measurements ( $\mathbf{x}^R$ ) and so-called nuisance parameters ( $\theta^R$ ) that influence the scattered power but are not of primary interest to the measurement are

$$\mathbf{x}^R = [\eta, \lambda_i]^T, \quad \theta^R = [T_g, \tau, p_g], \quad (2)$$

where  $\eta$ ,  $\lambda_i$ ,  $T_g$ ,  $\tau$ , and  $p_g$  are the system efficiency calibration constant, incident laser wavelength, neutral gas temperature, full-width half maximum of the spectral redistribution function, and neutral gas pressure, respectively. The governing equations describing the relationship between the LRS scattering spectrum and parameters ( $P_\lambda^R(\mathbf{x}^R, \theta^R)$ ) are given in Suazo Betancourt *et al.*<sup>50</sup>

In all LRS cases, data were collected from air at a single local barometric-pressure-corrected value of 5 Torr. LRS was collected with an incident laser energy of 500 mJ/pulse and a spectrometer slit width of  $500 \mu\text{m}$ . The signal from 50 laser pulses were



25 September 2024 16:36:34

**FIG. 3.** Master optical diagram for the interrogation, collection and detection systems.  $M$ ,  $i$ ,  $l$ ,  $PBS$ ,  $HWP$ ,  $BD$ ,  $PD$ ,  $PM$ ,  $F$  and  $BNF$  are acronyms for mirrors, irises, lenses, polarizing beam splitter cubes, half wave plates, beam dumps, photodiodes, power meters, and Bragg notch filters, respectively.  $I$ -,  $C$ - and  $D$ - indicate interrogation, collection, and detection, the axes to which the optical element corresponds to, respectively. The vacuum interface is represented as the red dashed line. This figure was reproduced from Suazo Betancourt *et al.*, J. Appl. Phys. **135**, 083302 (2024). Copyright 2024 AIP Publishing LLC. Reference 45 contains more thorough details on the layout presented in this figure.

accumulated on the camera sensor prior to each frame readout to maximize signal-to-noise, with 120 frames acquired at each calibration condition for a total of 6000 laser pulses. In general, data were acquired in order to maximize on-ccd accumulations. Then averaging over several tens to hundreds of frames once the maximum number of on-ccd accumulations were reached due to saturation. The number of total averaged pulses and the combination of on-ccd accumulations and averaged frames will be specified per LTS experiment because, in all LTS cases, on-ccd accumulations were limited by plasma emission lines. The fiber bundle illuminated about 300 pixels in the direction perpendicular to the wavelength-calibrated axis. On-chip binning was used in the direction perpendicular to the wavelength axis to minimize read noise

and improve signal-to-noise ratio (SNR). Binning along the wavelength-calibrated axis was not used to maintain spectral resolution. An invertible LRS spectrum was obtained from the measurements after subtraction of a background spectrum with the laser off.

LTS is the elastic electromagnetic scattering of incident radiation from unbounded charged particles and can be coherent or incoherent. Van de Sande<sup>51</sup> and Vincent<sup>52</sup> discuss the parameters determining whether an experimental setup and plasma conditions meet the conditions for coherent Thomson scattering; incoherent LTS is relevant here. For LTS, the wavelengths of the scattered radiation are consistent with the Doppler-shifted motion of the individual electrons along the scattering wave vector  $\mathbf{k}$ .<sup>52,53</sup> This is

directly linked to the relative velocity of the observer and the scattering electron along the scattering wave vector, viz.  $\mathbf{k} \equiv \mathbf{k}_i - \mathbf{k}_s$ , with  $\mathbf{k}_i$  being the incident propagation wave vector and  $\mathbf{k}_s$  being the wave vector along the direction from the scattering volume to the observer.

The scattering redistribution for unbound electrons happens over a spectral range of tens of nanometers, which is more than an order of magnitude larger than the spectrometer instrument function; instrument broadening of the measured spectra can be neglected. Hence, the total scattered power is redistributed over the spectral band dictated by the electron velocity distribution function (EVDF) along the scattering wave vector. For a plasma whose electron population is in thermal equilibrium, the spectral distribution function  $S_k(\lambda)$  corresponds to a Maxwellian EVDF that can be related to the equilibrium electron temperature  $T_e$ ; the classical electron temperature is the full descriptor for the shape of the distribution in such plasmas.<sup>52,54</sup> There are several analytical models that can be applied for non-equilibrium plasmas, including bi-Maxwellian and Druyvesteyn distributions.<sup>55–58</sup> Here, we do not pre-assume a form of the EVDF, but allow the plasma model selection to be supported by the data as described below. The governing Maxwellian and Druyvesteyn model equations ( $P_\lambda^T(\mathbf{x}^T, \theta^T)$ ) fit to the LTS signals can be found in Suazo Betancourt *et al.*,<sup>50</sup> and are parameterized by the QoI and nuisance parameter vectors,

$$\mathbf{x}^T = [T_e, n_e, v_d]^T, \quad \theta^T = [\eta, \lambda_i]^T, \quad (3)$$

with  $T_e$ ,  $n_e$ ,  $v_d$  being the electron temperature, electron density, and the magnitude of the bulk drift velocity along the scattering wave vector, respectively. Note that the scattering wave vector is not guaranteed to be parallel to any particular hardware feature of an experimental configuration. In our case, the scattering wave vector has a component parallel to the thruster axial axis and one parallel to the thruster radial or axial direction, depending on the location probed on the thruster. For a reconciliation between the scattering wave vector and the thruster axis vectors, see Refs. 59 and 60.

In general, four spectra are required in order to produce an invertible LTS spectrum. In addition to the desired LTS data, measurements are required to remove plasma emission, stray light from sources other than the plasma and elastic laser scattering, several sources of noise, and the detector background bias. These signals are typically collected with the laser on and the plasma on, laser on and the plasma off, laser off and the plasma on, and finally laser off and the plasma off, respectively. All background corrections other than the one for stray light were addressed in Suazo Betancourt *et al.*<sup>34</sup>

The main source of stray light in the current experiments is laser induced fluorescence, generated when the measurement volume is close to fluorescent material in the thruster hardware.<sup>52</sup> This fluorescence is red-shifted relative to the laser wavelength but still overlaps with the spectral range of the Thomson scattering at the conditions of interest. The magnitude of the stray light changes with the measurement of spatial location and laser parameters. Hence, a stray light correction image was taken at every measurement location (with the plasma off) using the same laser power and imaging settings as the LTS. Similar to Vincent,<sup>52</sup> the magnitude of the fluorescence spectra increased linearly with wavelength from about 539 nm to the highest wavelength measured. This linear fit was used to correct the measured LTS spectra for

fluorescent stray light at every measurement location. Further details of the correction are described in Lopez-Uricoechea *et al.*<sup>59</sup>

All measured signals—both LRS and LTS spectra—were inverted to find the QoI (and nuisance parameters) using a Bayesian framework.<sup>50</sup> The advantage of the Bayesian framework compared to more common least-squared analysis lies in its rigorous propagation and quantification of uncertainty through the entire signal inversion process, from the LRS through the LTS. Furthermore, in the LTS inversion, the Bayesian framework provides a rigorous assessment on the reliability of the plasma model underlying the signal inversion via the Bayes' factor. Hence, the result of the LRS or LTS signal inversion process is a posterior probability density function (PDF)  $\mathbb{P}^i(\mathbf{x}^i, \theta^i | \mathbf{b})$  following Bayes' equation,

$$\mathbb{P}^i(\mathbf{x}^i, \theta^i | \mathbf{b}) = \frac{\mathbb{P}^i(\mathbf{b} | \mathbf{x}^i, \theta^i) \mathbb{P}^i(\mathbf{x}^i, \theta^i)}{\mathbb{P}(\mathbf{b})}. \quad (4)$$

Here,  $\mathbb{P}^i(\mathbf{b} | \mathbf{x}^i, \theta^i)$ ,  $\mathbb{P}^i(\mathbf{x}^i, \theta^i)$ , and  $\mathbb{P}(\mathbf{b})$  are the likelihood, prior, and evidence PDFs,  $\mathbf{b}$  is the data for a given measurement, and  $i$  indicates whether the PDFs and parameters pertain to a LRS measurement ( $i = R$ ), LTS measurement inverted using a Maxwellian plasma model ( $i = TM$ ), etc. The posterior is a comprehensive description of one's knowledge of the QoI following a measurement, carrying all the measured and prior information about the QoI and nuisance parameters.

In this work, the likelihood distributions, parameters used to construct the prior probability distribution functions, etc. are the same as in Suazo Betancourt *et al.*<sup>50</sup> The posterior estimates from the LRS inference are used to construct the priors for the nuisance parameters for the LTS inference. This method robustly encodes the uncertainty in the neutral background pressure, neutral background temperature, center wavelength, and efficiency constant in the uncertainty for the electron temperature, density, and drift velocity. The PDFs were sampled using a Markov-chain Monte Carlo method. For the sake of computational efficiency, the length of the Markov chains was limited to 50 000 samples from the posterior using a Metropolis-Hastings algorithm. These samples were used to determine the maximum *a posteriori* (MAP) estimates of the QoI and quantify the uncertainty. In the results that follow, individual data points are the MAP values of the QoI and the error bars represent plus and minus twice the standard deviation for each parameter.

For all LTS measurements, signals were inverted using both Maxwellian and Druyvesteyn plasma models. From these, we compute the Bayes' factor,

$$B_{2,1} = \frac{\mathbb{P}(\text{Druyvesteyn} | \mathbf{b})}{\mathbb{P}(\text{Maxwellian} | \mathbf{b})}, \quad (5)$$

as a measure of the support for the Maxwellian vs Druyvesteyn EVDF submodels. Details on Bayes' factor and plasma model selection across several plasma submodels are described Sec. III D of Suazo Betancourt *et al.*<sup>50</sup> In what follows, we report  $\ln(B_{2,1})$ , where  $\ln(B_{2,1}) < -1$  indicates that the data strongly support the Maxwellian plasma model and  $|\ln(B_{2,1})| \leq 1$  indicate that the data could equally be from a Maxwellian or Druyvesteyn plasma.



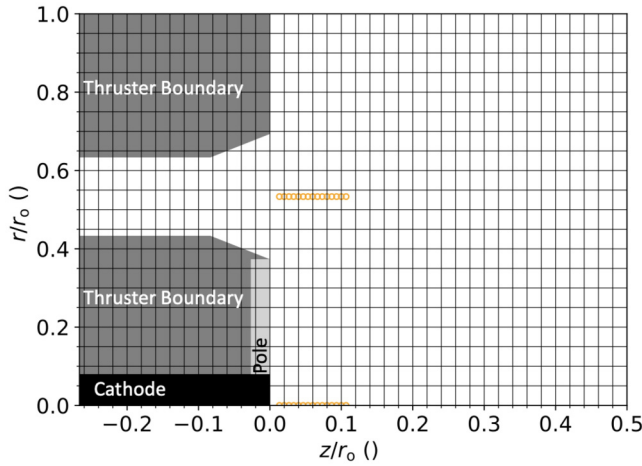


FIG. 4. Normalized discharge channel and cathode axial measurement locations. The thruster boundaries are represented in gray, the front pole cover in light gray, and the cathode keeper body in black. The thruster extends no further than  $r_0 = 1$ . Note that the relative size of the glyphs is not to scale, and all measurement locations are at a separate location exceeding the positional uncertainty of the system.

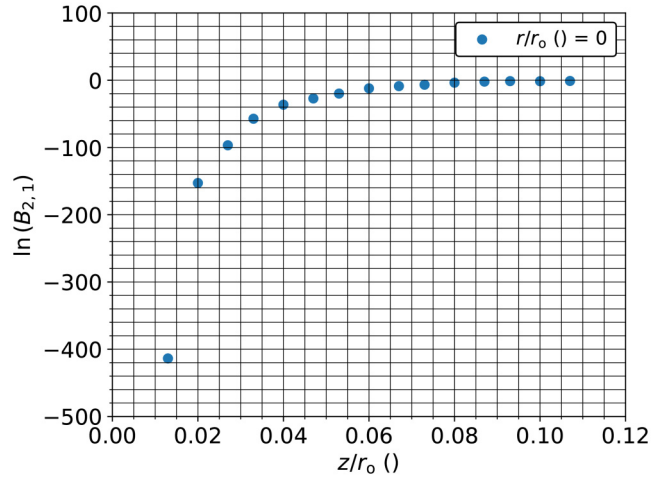


FIG. 5. Spatially normalized axial profile of the Bayes' factor for the Maxwellian and Druyvesteyn submodels  $\ln(B_{2,1})$ .

### III. RESULTS AND DISCUSSION

#### A. Discharge channel and cathode centerline axial measurements

The measurement locations for this experiment are presented in Fig. 4, with one set of measurements extending in the  $z$ -direction along the cathode (and hence thruster) centerline ( $r/r_0 = 0$ ) and one along the discharge channel mid-radius. The average facility operational pressure ( $P_O$ ), anode mass flow rate ( $\dot{m}_A$ ), cathode mass flow rate ( $\dot{m}_C$ ), discharge voltage ( $V_D$ ), discharge current ( $I_D$ ), and the peak frequencies for the discharge circuit ( $f_{V_D}, f_{I_D}$ ), respectively, are tabulated in Table I.

The cathode axial centerline data were collected at an incident laser energy of 1 J/pulse using a total of 3000 laser pulses at each location. These pulses were accumulated on between 30 and 600 individual frames, depending on the signal level that caused sensor saturation. The thruster discharge channel mid-radius data was collected at the thruster 12 o'clock position azimuthally at an incident laser energy of 1 J/pulse. For these data, which had less variation in number density and signal-to-noise, 40 frames were collected with each frame accumulating 150 laser pulses for a total of 6000 laser pulses per location.

Figure 5 shows the Bayes' factor for the cathode centerline measurements, demonstrating that the data support a Maxwellian plasma model. That is,  $\ln(B_{2,1}) < -1$  for all data and is much less than negative one for the points close to the thruster. Note that the reduced signal-to-noise ratio as the distance from the thruster increased resulted in less clear support for the Maxwellian model, but there was no support for the Druyvesteyn model in the data.

The profiles of electron properties along the cathode centerline and channel mid-radius, calculated using the Maxwellian plasma model, are presented in Figs. 6 and 7. The electron number density along the cathode centerline decreased by two orders of magnitude over the measured distance, whereas the channel mid-radius number density decreased by approximately 85%. In both cases, monotonic decreases in the electron number density were expected. The outliers at  $z/r_0$  of 0.013 and 0.027, and hence non-monotonic trend, in the channel electron number density is attributed to inaccurate realignment of the fiber image on the laser beam after facility movement. The skewed uncertainty bounds for these points are based on estimated collection efficiency deficits with misaligned optics during an acquisition, quantified through successively misaligning the fiber image with respect to the beam until and signal was at a minimum at a single spatial point.

The electron temperature increases by factors of approximately two and three along the cathode centerline and channel mid-radius, respectively, to a maximum of approximately 30 eV at its

TABLE I. Hall effect thruster discharge telemetry for the discharge channel and centerline, cathode grid, and discharge channel/front pole grid experiments, respectively.

Experiment	$P_O$ (Torr Kr)	$\dot{m}_A$ (mg/s)	$\dot{m}_C$ (mg/s)	$V_D$ (V)	$I_D$ (V)	$f_{V_D}$ (kHz)	$f_{I_D}$ (kHz)
Centerline	$6.6 \times 10.0^{-6} \pm 3.6\%$	$23.9 \pm 1.0\%$	$1.7 \pm 1.0\%$	$150.8 \pm 8.7\%$	$39.8 \pm 17.5\%$	$6.5 \pm 1.0\%$	$6.5 \pm 1.0\%$
Cathode grid	$7.5 \times 10.0^{-6} \pm 1.1\%$	$24.2 \pm 1.0\%$	$1.8 \pm 1.0\%$	$150.2 \pm 4.7\%$	$39.7 \pm 16.9\%$	$6.4 \pm 1.8\%$	$6.3 \pm 1.6\%$
Channel/pole grid	$6.8 \times 10.0^{-6} \pm 1.4\%$	$23.9 \pm 1.0\%$	$1.7 \pm 1.0\%$	$149.7 \pm 4.1\%$	$40.5 \pm 16.6\%$	$6.4 \pm 1.8\%$	$6.3 \pm 1.9\%$

25 September 2024, 16:36:34

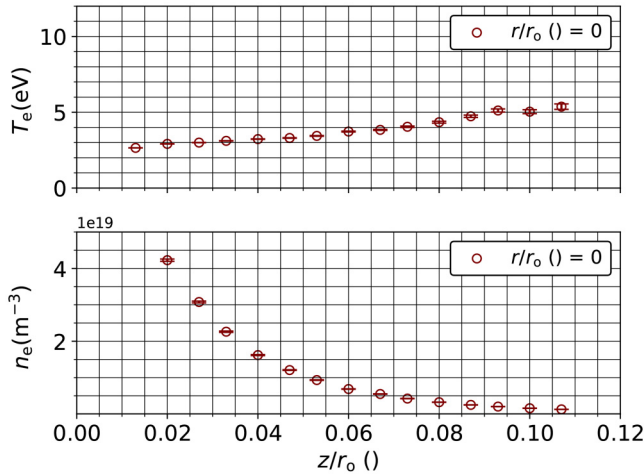


FIG. 6. Spatially normalized electron temperature and density profiles at the cathode centerline using a Maxwellian submodel.

peak. The magnitude of the electron temperature (in eV) is approximately 20% of the discharge voltage (in V). In contrast, empirical scaling relationships based on previous high-speed probe measurements indicate that the maximum electron temperature in this thruster should be around 10%–15% of the discharge voltage.<sup>35,61–63</sup> However, our measurements are consistent with other LTS data collected in the plume of other thrusters that also reach peak temperatures of approximately 20% (in eV) of the discharge voltage (in V),<sup>52,60</sup> indicating a need to reassess the aforementioned correlations that provide lower peak electron temperatures than are being measured by LTS. We expect that these discrepancies are due to perturbations in the plasma caused by physical probes, e.g., as shown by Ryan *et al.*<sup>64</sup> Additionally, the

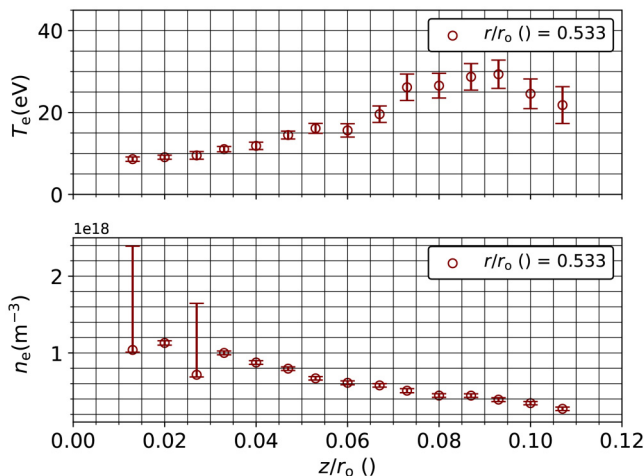


FIG. 7. Spatially normalized electron temperature and density profiles at the channel centerline using a Maxwellian submodel.

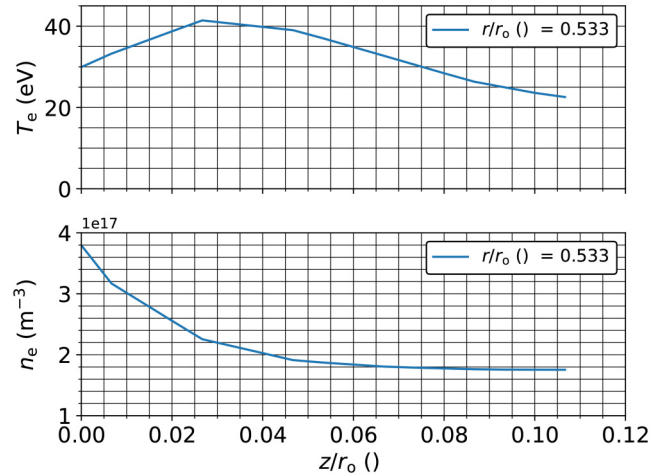


FIG. 8. Channel centerline electron temperature and density profiles based on the simulations of Marks and Jorns.<sup>65</sup>

maximum temperature along the cathode centerline is approximately half the minimum temperature along the thruster channel mid-radius, consistent with expectations.

Currently, there are no simulations of this HET at 40 A, 150 V available. However, Hall2De simulations<sup>65</sup> of the nominal 4.5-kW condition at 15 A, 300 V may be used for a qualitative comparison. Figure 8 presents the normalized electron property profiles along the channel centerline from these simulations.

A comparison of limited available ion-property-calibrated simulation data, electrostatic probe measurements, and LTS measurements across several previous studies was conducted to legitimize the measured electron temperatures for the purposes of drawing conclusions from our data. The 4.5-kW Hall2De simulations<sup>65</sup> indicate a peak centerline temperature (in eV) that is about 13% of the discharge voltage (in V). The simulations in Ref. 30 show a peak temperature (in eV) that is approximately 10% of the discharge voltage (in V). This is consistent with the measurements from Haas<sup>62</sup> that indicate a peak temperature (in eV) of approximately 10% of the discharge voltage (in V) 300 V at 5.4 and 10 A. These measurements also implied insensitivity of the peak electron temperature to mass flow rate.<sup>62</sup>

The agreement between the simulations and electrostatic probe measurements across two different thrusters operating at similar current densities suggests peak electron temperatures of 10–15% (in eV) of the discharge voltage to be expected. We are interested in scaling this to our 150 V, 40 A case, keeping in mind that the limited data for parametric variation in the thruster operating point for deriving empirical scaling other than of Haas.<sup>62</sup> This scaling leads to an expected electron temperature of 15–22.5 eV. However, we observed a peak temperature of approximately 30 eV. Review of other LTS work, from Vincent<sup>52,60,66</sup> and Roberts,<sup>33,35</sup> the peak electron temperature is expected to be higher than that predicted from the electrostatic and simulation scaling, at approximately 20% (in eV) of the discharge voltage (in V). There is a lack of electron calibration data for simulations. This would suggest that the

25 September 2024 16:36:34

**TABLE II.** Hall effect thruster discharge telemetry for the constant power discharge experiment at  $z/r_o = 0.013$ .

$P_O$ (Torr Kr)	$\dot{m}_A$ (mg/s)	$\dot{m}_C$ (mg/s)	$V_D$ (V)	$I_D$ (V)	$f_{V_D}$ (kHz)	$f_{I_D}$ (kHz)
$3.9 \times 10.0^{-6}$	$14.5 \pm 1.0\%$	$1.70 \pm 1.0\%$	$300.2 \pm 2.5\%$	$20.3 \pm 81.0\%$	$14.3 \pm 1.0\%$	$14.3 \pm 1.0\%$
$4.38 \times 10.0^{-6}$	$15.9 \pm 1.0\%$	$1.70 \pm 1.0\%$	$240.0 \pm 2.9\%$	$24.9 \pm 42.2\%$	$10.7 \pm 2.7\%$	$10.7 \pm 2.7\%$
$5.13 \times 10.0^{-6}$	$18.2 \pm 1.0\%$	$1.72 \pm 1.0\%$	$201.5 \pm 3.3\%$	$29.8 \pm 19.6\%$	$7.50 \pm 4.2\%$	$7.50 \pm 4.2\%$
$6.00 \times 10.0^{-6}$	$21.4 \pm 1.0\%$	$1.72 \pm 1.0\%$	$172.5 \pm 3.5\%$	$35.1 \pm 13.0\%$	$7.10 \pm 5.1\%$	$7.10 \pm 5.1\%$
$6.85 \times 10.0^{-6}$	$23.8 \pm 1.0\%$	$1.70 \pm 1.0\%$	$148.6 \pm 4.7\%$	$39.7 \pm 20.0\%$	$6.60 \pm 2.0\%$	$6.60 \pm 2.0\%$

deviation in the scaling between LTS compared to ion-data-calibrated simulations and electrostatic probe measurements may not only be related to the perturbative nature of the probes but related to ion velocity data from LIF used to calibrate the simulations.

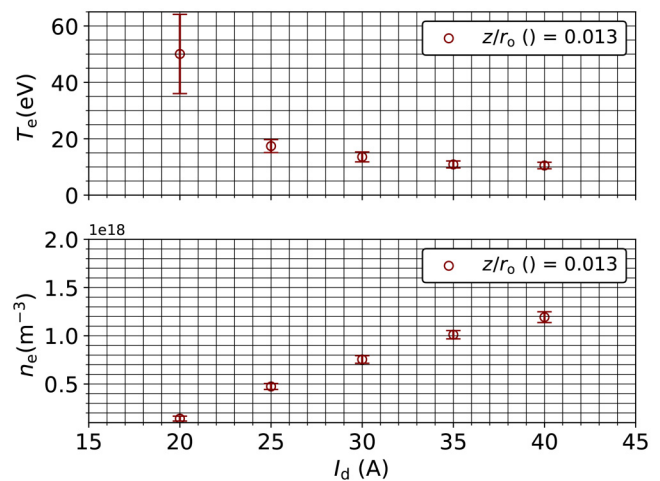
In addition to understanding the measured magnitude of the electron temperature, a comparison of the location of the peak electron temperature allows further analysis of the discharge plasma. The 4.5 kW simulations indicate peak temperature before the expected peak in the axial magnetic field, as opposed to our results that indicate the peak temperature to be after the peak in the magnetic field, whose axial peak along the discharge channel centerline was located approximately  $z/r_o = 0.065$ .<sup>46</sup> Previous simulation and experimental efforts indicate that the expected peak temperature is approximately located at the point of maximum axial electric field strength,<sup>67</sup> and is approximately coincident with the axial location of the maximum magnetic field with temperatures increasing to this point due to Joule heating near the maximum magnetic field.<sup>26</sup> However, this location is expected to be shifted between magnetically shielded and unshielded architectures,<sup>25,60</sup> justifying our downstream-shifted peak electron temperature relative to the peak magnetic flux density location. The shift in the maximum temperature from the experimentally measured data at 150 V, 40 A, and the 4.5-kW simulations suggests that at lower voltage and higher current densities, the acceleration region is shifted further downstream axially. This agrees with ion velocity distribution function measurements showing the downstream movement of the acceleration region at lower discharge voltages.<sup>68</sup> The location of the peak temperature in Roberts and Jorns<sup>35</sup> being closer to the discharge channel exit plane than our peak temperature is consistent with this as well, given the higher discharge voltage. In the work by Peterson *et al.*,<sup>11</sup> the 12.5-kW thruster was tested with the thruster floating, thruster body tied to facility ground, and thruster body tied to facility ground with conducting and dielectric discharge channels. The location of the acceleration region and its variation with electrical configuration was a key conclusion from the work. This results indicates the need to verify these trends at several thruster electrical boundary conditions.

Data taken at a normalized axial distance of  $z/r_o = 0.013$ , while maintaining a constant power of 6 kW and constant absolute coil currents, can help to provide initial insights into the relative peak temperatures and number densities between the 4.5-kW simulation and the 6-kW axial profile. Data were collected at a constant discharge power of 6 kW, and operating conditions are tabulated in Table II.

Figure 9 presents the electron temperature and density as a function of the discharge current at a constant power of 6 kW.

These profiles suggest monotonically decreasing temperatures and monotonically increasing number density with increasing flow rates and decreasing discharge voltage at constant power. The simulated electron density in the 400 V, 15 A simulations is approximately  $4 \times 10^{17} \text{ m}^{-3}$  and the measured electron density at 20 A, 300 V is less than  $1 \times 10^{17} \text{ m}^{-3}$ , indicating an over prediction of the simulated electron density. However, the over prediction may be due to several reasons that are not yet clear; the method used to calibrate the simulation parameters, poorly understood phenomena like the effect of anomalous electron mobility and thruster instabilities, or the unlikely case of systematic errors in the number density estimation across the several groups using LTS for similar experiments.

The measured electron temperature of approximately 50 eV at 300 V, 20 A is reasonable when compared to simulated temperature of approximately 37 eV at 300 V, 15 A given the aforementioned scalings. The difference in temperature between the 20 A and 15 A cases is expected to be because of the lower mass flow rate in the former case, resulting in a higher temperature.<sup>69</sup> However, the difference in the predicted and measured electron number densities—specifically the over-prediction of the maximum electron number

**FIG. 9.** Electron temperature and density vs discharge current with a constant power of 6 kW at the channel centerline at a normalized axial location of  $z/r_o = 0.013$ .

density—motivates a parametric study of the axial profile of the electron temperature and density as a function of discharge voltage and current, similar to the work in Roberts *et al.*,<sup>70</sup> spanning into the high current density domain. The qualitative and quantitative comparisons made in this section give us confidence in our measured results in order to draw conclusions from the measurements in Secs. III B and III C.

### B. Discharge channel, front pole and cathode grid measurements

The measurement locations for these experiments are presented in Fig. 10. These experiments were carried out over two thruster shut-downs and vacuum breaks. The near-field cathode grid points were acquired together, and the thruster and front pole grid points were acquired together. The facility operational parameters are tabulated in Table I.

The cathode grid data, shown with square markers in Fig. 10, were collected along the 12 o'clock radial slice between the cathode centerline to the edge of the cathode keeper. The data were collected at incident laser energies between 730 and 760 mJ/pulse, with a total of 1500 laser pulses accumulated at each condition on 50–100 individual frames. The decrease in laser energy was due to decreasing laser performance over the long duration of the experimental campaign, not due to any diagnostic necessity. The total number of laser pulses at each point was reduced compared to the results presented above to facilitate a denser grid near the cathode while managing total data collection time. Periodic realignment of the fiber image with respect to the beam plane allowed for more consistent optical calibration during this experiment. Between each

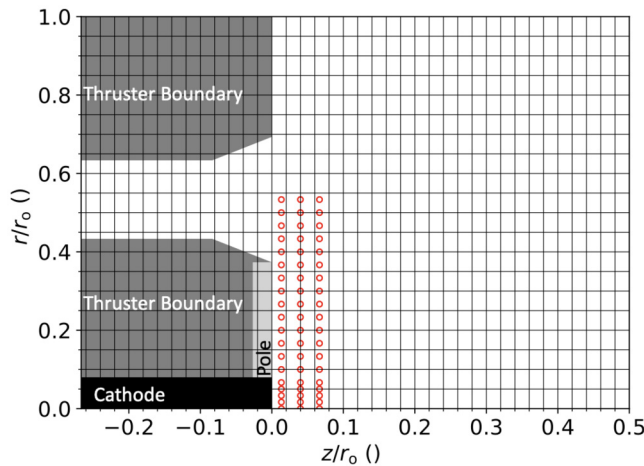


**FIG. 10.** Normalized discharge channel, front pole, and cathode grid measurement locations. The thruster boundaries are represented in gray, the front pole cover in light gray, and the cathode keeper body in black. The thruster extends no further than  $r_o = 1$ . Note that the relative size of the glyphs is not to scale, and all measurement locations are at a separate location exceeding the positional uncertainty of the system.

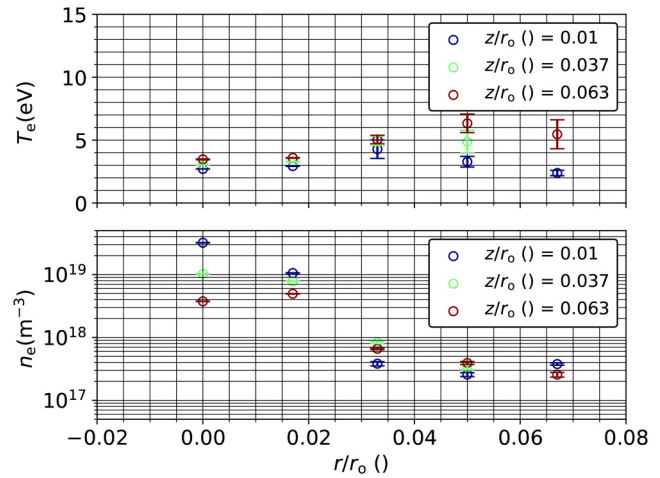


**FIG. 11.** Spatially normalized electron temperature and density profiles for the cathode grid.

measurement location, the thruster was returned to the nearest cathode centerline point and the fiber image realigned with respect to the beam. However, this procedure introduced an additional average positioning uncertainty of approximately 200  $\mu\text{m}$  in addition to the minimum positioning uncertainty of 150  $\mu\text{m}$  inherent to the motion stages.

The spatially normalized electron temperature and density profiles for the cathode grid are presented in Fig. 11. The temperature increased with increasing radius to  $r/r_o$  of about 0.05, then decreased. Additionally, the temperature increased with axial location away from the keeper orifice. The number density decreased with increasing radial distance. However, there is a switch in the trend with increasing axial distance. In the core plasma in front of the cathode orifice, up to  $r/r_o$  of approximately 0.02, the density decreases with increasing axial distance. However, in front of the cathode keeper boundary, the density increases with axial distance. This suggests the existence of a background plasma between the cathode orifice and discharge channel that can create a conductive path for particles to the thruster and cathode surfaces. Note that it is difficult to distinguish a trend with axial position at the highest  $r/r_o \approx 0.065$  due to the relatively constant values.

The first acquisition of the discharge channel and front pole grid data, collected along the thruster 12 o'clock radial slice did not show consistent electron number density trends due to misalignment artificially reducing the number density. It was discovered that the thermal state of the lens inside of the chamber at energies above 500 mJ/pulse affected the alignment more frequently than anticipated. Therefore, the thruster 12 o'clock radial slice was abandoned for the thruster 3 o'clock radial slice because the cathode centerline realignment at the thruster 12 o'clock radial slice was limited by the speed of the vertical motion stage. At the 3 o'clock radial slice, the system could be realigned quickly. For the remainder of the experiments, the system was realigned between every point. The discharge channel and front pole grid data, shown with

25 September 2024 16:36:34

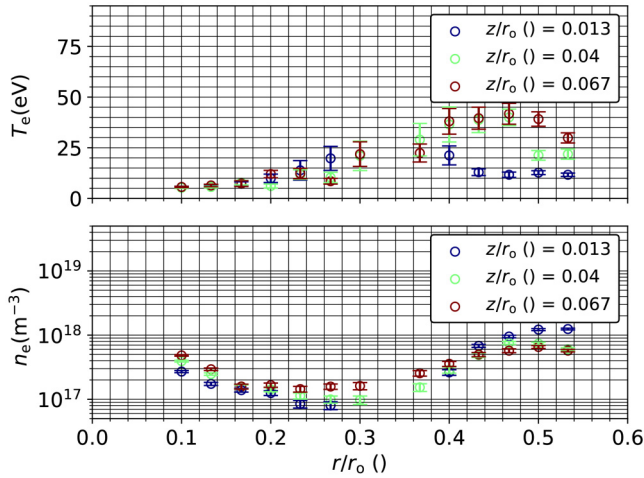


FIG. 12. Spatially normalized electron temperature and density profiles for the channel and front pole grid.

square markers in Fig. 10, was collected along the 3 o'clock radial slice. The incident laser energies varied between 620 and 770 mJ/pulse with the number of frames averaged varied from 40 to 10 with a total number of 3000 laser pulses. This was done to maximize the number of points collected and to minimize the dwell time between realignment of the fiber image. The spatially normalized electron temperature and density profiles for the channel and pole grid are presented in Fig. 12.

The electron density decreased monotonically with both distance away from the channel mid-radius and axial distance. This is expected due to the combination of expansion from the higher neutral pressure discharge channel region into the vacuum environment. The temperature close to the exit of the discharge channel remained low, increasing toward the channel edge at  $r/r_o \approx 0.4$ . At larger axial distances, the temperature increased and then decreased toward the front pole region from the channel edge. The temperature toward the edge of the channel at distances of  $r/r_o$  between 0.36 and 0.5 decreased radially toward the pole but had less variation axially.

At the discharge channel centerline ( $r/r_o = 0.533$ ), the flux density is about 66% less strong than in the front pole region ( $r/r_o = 0.267$ ).<sup>46</sup> The increase in magnetic flux density toward the channel edge and into the front pole region suggests a region of highly magnetized electrons that can quickly thermalize. This is evidenced by the loss in axial sensitivity to the electron temperature at  $r/r_o$  between 0.36 and 0.5.

### C. Discharge channel and front pole analysis

Electron pressures ( $P_e$ ) were calculated from the measured electron temperatures and number densities; the  $P_e$  distribution is visualized in Figs. 13 and 14. Assuming a single ion species denoted by  $i$ , using an isotropic closure for the pressure tensor and a frictional-like collisional model for the viscosity tensor, and assuming negligible electron momentum along with a minimal

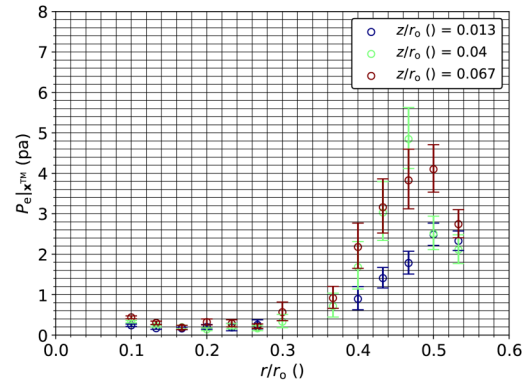


FIG. 13. Electron pressure profiles in the channel and front pole grid.

contribution of the Hall current in the  $r - z$  plane, the electron momentum equation yields

$$\mathbf{E} = \frac{1}{n_e q_e} [\nabla P_e - v_{e/i} m_e n_e (\mathbf{u}_e - \mathbf{u}_i)], \quad (6)$$

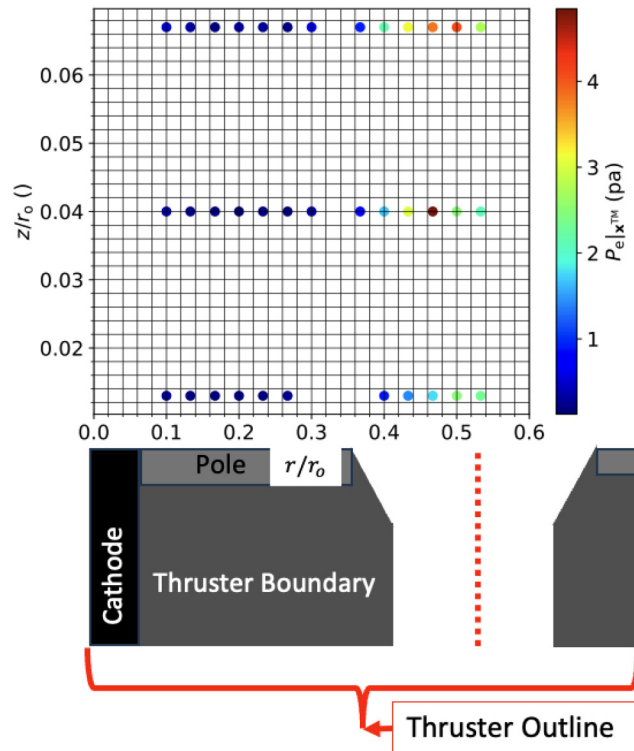


FIG. 14. Spatial heat map of the channel and front pole grid electron pressure.

25 September 2024 16:36:34

where  $\mathbf{E}$ ,  $v_{e/i}m_e$ ,  $n_e$ ,  $\mathbf{u}_e$ , and  $\mathbf{u}_i$  are the electric field, the total electron-ion collision frequency, the electron mass, and the electron and ion velocities, respectively.

The inability to accurately model the collisional terms due to anomalous electron mobility in areas of high magnetic flux density, specifically approaching the front pole region, limits our ability to analytically solve for the electric field. This challenge is discussed in works by Mikellides *et al.*<sup>29</sup> and Marks *et al.*<sup>31,71</sup> The works by Mikellides *et al.*<sup>29,30,72</sup> do not suggest bounds for this collisional term. The works by Marks *et al.*<sup>31,71</sup> suggest that an understanding of cross field electron mobility would allow for accurate models for this term. However, at present, cross-magnetic field electron mobility is poorly understood. Work by Suazo Betancourt *et al.*<sup>73</sup> suggests that fundamental studies of electron transport along and across magnetic field lines would provide insights into this cross field transport. Therefore, ignoring the collisional term yields

$$\mathbf{E} = \frac{1}{n_e q_e} \nabla P_e. \quad (7)$$

That is, in the absence of collisional terms, the trend in the electric field is expected to follow the trend in the electron pressure gradient to within the limitations of the assumptions previously stated.

The electron pressure for the discharge channel and pole grid is minimum between  $r/r_0$  of 0.2–0.3 and constitutes the lowest electron pressure of the entire system between the discharge channel and cathode centerlines, including that of less than  $z/r_0$  0.08 pertaining to the cathode. Additionally, we estimate that the acceleration region, in this case, is located approximately between  $z/r_0$  of 0.08–0.1 according to the axial profiles of the electron temperature and the peak temperatures at this condition.<sup>16,22</sup> These electron pressure profiles, with a minimum immediately ahead of the front pole, along with the approximate location of the acceleration region that has been estimated to be shifted downstream of the exit plane, indicate that axially-unaccelerated centerline and beam edge ions can be accelerated to the pole, contributing to pole erosion. Jorns *et al.*<sup>16</sup> found that the ion population immediately ahead of the pole did not have sufficient energy to erode the poles at the observed rate. Small quantities of ions originating from the beam core and edge where the electron temperature is observed to exceed 25 eV could lead to multiply charged ions. This would have a significant impact on the erosion in this region as erosion models predict highly nonlinear erosion rates with both ion species and energy.<sup>74</sup> Whether these observations are true for all operating conditions, especially at higher voltages where the acceleration region is expected to recess toward the thruster exit plane,<sup>35</sup> remains to be confirmed.

#### IV. CONCLUSIONS

Modifications to the interrogation beam optical axis and the collection acquisition strategy as well as data pre-processing presented in Ref. 34 allowed for measurements traversing the front pole region from the discharge channel centerline to the cathode centerline in the near field plume of an MS HET operating at high current densities and low voltage. This, coupled with the work in Ref. 34 contributes to one of the first detailed, modifiable, and

repeatable large vacuum test facility LTS systems in the literature to date. This paper presents the first measurements with full optical access to the plasma immediately ahead of the front pole region and one of the first sets of measurements to probe the discharge channel centerline with an exposed acceleration region.<sup>59</sup>

The measurements along the discharge channel and cathode centerlines have shapes that agree with first-principles-based plasma simulations. The location of the peak temperature region suggests downstream movement of the acceleration region at the given discharge condition, which also agrees with LIF measurements indicating movement of the expected location of the acceleration region with decreasing voltage. These measurements open up the ability for parametric discharge channel centering measurements at different voltage and mass flow rates for calibration of simulations and comparison of simulations calibrated with electron properties from LTS vs ion properties from LIF.

Analysis of the spatially resolved data traversing the front pole concluded that within the limitation of the analysis discussed in Sec. III C, it agrees with LIF ion velocity measurements, indicating that unaccelerated ions from the discharge channel and beam edges can be accelerated toward the pole. This contributes some of the first-ever measurements and analysis traversing regions with a minimally invasive diagnostic that are critical to understanding the life limiting phenomena in MS HETs—pole erosion. This, coupled with the possible acceleration region shifts, may be the reason to conclude that higher current density architecture MS HETs may suffer from higher pole erosion rates. However, this will require further investigations to confirm.

The work in this paper provides some of the first insights into regions that have been difficult to probe with confidence using traditional measurement techniques in the EP community due to advancements in laser-based diagnostics. This provides an avenue for future minimally invasive work that can help contribute to the understanding of the near-field plasma environment from the perspective of the electrons. Given that electrons are much more mobile than ions due to their mass difference, it is expected that electrons play a governing role in the plasma dynamics in HETs. This will allow for the contribution of data for the calibration of simulations and validation of models for unknown terms in physics-based closures in simulations. This will contribute to the predictive design of HETs through simulations that are ever more reliable given an updated understanding of the electron contributions to the plasma. For regions that have phenomena of interest that contribute to the life-limiting factors of HETs, like the front pole region, measurements like the ones made in this paper will help understand these life-limiting mechanisms and predict their long-term effect on HETs more accurately. This will, in turn, minimize the design and testing efforts for HETs. The work in this paper provides some of the first steps toward these goals.

#### ACKNOWLEDGMENTS

The authors would like to thank Professor Samuel J. Grauer for his contributions to the Bayesian framework used in the processing of the data in this manuscript.

## AUTHOR DECLARATIONS

## Conflict of Interest

The authors have no conflicts to disclose.

## Author Contributions

**Jean Luis Suazo Betancourt:** Conceptualization (lead); Formal analysis (lead); Methodology (lead); Software (lead); Visualization (lead); Writing – original draft (lead); Writing – review & editing (lead). **Julian Lopez-Uricoechea:** Conceptualization (equal); Formal analysis (equal); Methodology (equal); Software (equal); Visualization (equal); Writing – original draft (equal); Writing – review & editing (equal). **Naia Butler-Craig:** Conceptualization (equal); Formal analysis (equal); Methodology (equal); Software (equal); Visualization (equal); Writing – original draft (equal); Writing – review & editing (equal). **Adam M. Steinberg:** Funding acquisition (lead); Project administration (lead); Supervision (lead); Writing – original draft (equal); Writing – review & editing (equal). **Mitchell L. R. Walker:** Funding acquisition (lead); Project administration (lead); Supervision (lead); Writing – original draft (equal); Writing – review & editing (equal).

## DATA AVAILABILITY

The data that support the findings of this study are available from the corresponding author upon reasonable request.

## REFERENCES

- <sup>1</sup>D. M. Goebel and I. Katz, *Fundamentals of Electric Propulsion: Ion and Hall Thrusters* (Wiley, 2008).
- <sup>2</sup>R. G. Jahn, *Physics of Electric Propulsion* (Dover, 2006), pp. 1–50, ISBN 978-0486450407.
- <sup>3</sup>V. V. Zhurin, H. R. Kaufman, and R. S. Robinson, *Plasma Sources Sci. Technol.* **8**, R1 (1999).
- <sup>4</sup>V. Kim, *J. Propul. Power* **14**, 736 (1998).
- <sup>5</sup>B. Pote, V. Hruby, and R. Tedrake, in *36th AIAA/ASME/SAE/ASEE Joint Propulsion Conference and Exhibit* (AIAA, 2006), pp. 3249.
- <sup>6</sup>S. E. Cusson, M. P. Georgin, H. C. Dragnea, E. T. Dale, V. Dhaliwal, I. D. Boyd, and A. D. Gallimore, *J. Appl. Phys.* **123**, 133303 (2018).
- <sup>7</sup>B. Beal, A. Gallimore, and W. Hargus, in *41st AIAA/ASME/SAE/ASEE Joint Propulsion Conference & Exhibit* (American Institute of Aeronautics and Astronautics, Reston, VA, 2005).
- <sup>8</sup>C. Chhavi and M. L. R. Walker, *J. Electric Propul.* (published online, 2024).
- <sup>9</sup>S. Y.-M. Cheng, “Modeling of Hall thruster lifetime and erosion mechanisms,” Ph.D. thesis (Massachusetts Institute of Technology, 2007).
- <sup>10</sup>X. Duan, D. Guo, M. Cheng, X. Yang, and N. Guo, *J. Appl. Phys.* **128**, 183301 (2020).
- <sup>11</sup>P. Y. Peterson, H. Kamhawi, W. Huang, G. Williams, J. H. Gilland, J. Yim, R. R. Hofer, and D. A. Herman, in *52nd AIAA/SAE/ASEE Joint Propulsion Conference* (AIAA, 2016), pp. 5027.
- <sup>12</sup>H. Kamhawi, T. Haag, W. Huang, J. Yim, D. A. Herman, P. Y. Peterson, G. Williams, J. Gilland, R. R. Hofer, and I. G. Mikellides, in *52nd AIAA/SAE/ASEE Joint Propulsion Conference* (American Institute of Aeronautics and Astronautics, Reston, VA, 2016).
- <sup>13</sup>S. Cusson, “Impact of neutral density on the operation of high-power magnetically shielded Hall thrusters,” Ph.D. thesis (University of Michigan, Ann Arbor, 2019).
- <sup>14</sup>I. G. Mikellides, I. Katz, R. R. Hofer, and D. M. Goebel, *Appl. Phys. Lett.* **102**, 023509 (2013).
- <sup>15</sup>I. G. Mikellides, I. Katz, R. R. Hofer, and D. M. Goebel, *J. Appl. Phys.* **115**, 043303 (2014).
- <sup>16</sup>B. A. Jorns, C. Dodson, J. Anderson, D. M. Goebel, R. R. Hofer, M. Sekerak, A. Lopez Ortega, and I. Mikellides, in *52nd AIAA/SAE/ASEE Joint Propulsion Conference, 2016* (AIAA, 2016).
- <sup>17</sup>I. G. Mikellides, R. R. Hofer, I. Katz, and D. M. Goebel, *J. Appl. Phys.* **116**, 053302 (2014).
- <sup>18</sup>M. Martínez-Sánchez and E. Ahedo, *Phys. Plasmas* **18**, 033509 (2011).
- <sup>19</sup>R. R. Hofer, D. M. Goebel, I. G. Mikellides, and I. Katz, *J. Appl. Phys.* **115**, 043304 (2014).
- <sup>20</sup>R. R. Hofer, B. A. Jorns, J. E. Polk, I. G. Mikellides, and J. S. Snyder, in *33rd International Electric Propulsion Conference* (Electric Rocket Propulsion Society, Washington D.C., 2013).
- <sup>21</sup>D. M. Goebel, B. A. Jorns, R. R. Hofer, I. G. Mikellides, and I. Katz, in *50th AIAA/ASME/SAE/ASEE Joint Propulsion Conference 2014* (AIAA, 2014).
- <sup>22</sup>I. G. Mikellides and A. L. Ortega, in *50th AIAA/ASME/SAE/ASEE Joint Propulsion Conference 2014* (AIAA, 2014).
- <sup>23</sup>A. L. Ortega, I. G. Mikellides, V. H. Chaplin, W. Huang, and J. D. Frieman, in *AIAA Propulsion and Energy 2020 Forum* (AIAA, 2020).
- <sup>24</sup>A. Lopez Ortega, I. G. Mikellides, M. J. Sekerak, and B. A. Jorns, *J. Appl. Phys.* **125**, 033302 (2019).
- <sup>25</sup>Z. Wang, H. Li, C. Zhong, J. Liu, Y. Ding, L. Wei, and D. Yu, *IEEE Trans. Plasma Sci.* **49**, 1351–1356 (2021).
- <sup>26</sup>J. C. Adam, J. P. Boeuf, N. Dubuit, M. Dudeck, L. Garrigues, D. Gresillon, A. Heron, G. J. Hagelaar, V. Kulaev, N. Lemoine, S. Mazouffre, J. Perez Luna, V. Pisarev, and S. Tsikata, *Plasma Phys. Controlled Fusion* **50**, 124041 (2008).
- <sup>27</sup>J. P. Boeuf, *J. Appl. Phys.* **121**, 011101 (2017).
- <sup>28</sup>L. Grimaud, A. Pétin, J. Vaudolon, and S. Mazouffre, *Rev. Sci. Instrum.* **87**, 043506 (2016).
- <sup>29</sup>I. G. Mikellides and A. L. Ortega, *Plasma Sources Sci. Technol.* **28**, 14003 (2019).
- <sup>30</sup>I. G. Mikellides and I. Katz, *Phys. Rev. E - Stat., Nonlinear, Soft Matter Phys.* **86**, 046703 (2012).
- <sup>31</sup>T. A. Marks and B. A. Jorns, *Plasma Sources Sci. Technol.* **32**, 045016 (2023).
- <sup>32</sup>P. J. Roberts, B. A. Jorns, and V. H. Chaplin, in *AIAA Scitech 2022 Forum* (American Institute of Aeronautics and Astronautics, Reston, VA, 2022).
- <sup>33</sup>P. J. Roberts and B. Jorns, in *AIAA Scitech 2023 Forum* (American Institute of Aeronautics and Astronautics, Reston, VA, 2023), pp. 1.
- <sup>34</sup>J. L. Suazo Betancourt, N. Butler-Craig, J. Lopez-Uricoechea, J. Bak, D. Lee, A. M. Steinberg, and M. L. R. Walker, *J. Appl. Phys.* **135**, 083302 (2024).
- <sup>35</sup>P. J. Roberts and B. A. Jorns, *Phys. Rev. Lett.* **132**, 135301 (2024).
- <sup>36</sup>A. W. Kieckhafer and M. L. R. Walker, in *32nd International Electric Propulsion Conference* (Electric Rocket Propulsion Society, Wiesbaden, 2011).
- <sup>37</sup>S. Dusuhman and J. M. Lafferty, *Scientific Foundations of Vacuum Technique*, 2nd ed. (John Wiley & Sons, 1958), ISBN - 10 0471228036.
- <sup>38</sup>R. R. Hofer, S. E. Cusson, R. B. Lobbia, and A. D. Gallimore, in *35th International Electric Propulsion Conference, Atlanta, GA* (Electric Rocket Propulsion Society, 2017).
- <sup>39</sup>S. J. Hall, R. E. Florenz, A. Gallimore, H. Kamhawi, D. L. Brown, J. E. Polk, D. M. Goebel, and R. R. Hofer, in *50th AIAA/ASME/SAE/ASEE Joint Propulsion Conference* (American Institute of Aeronautics and Astronautics, Reston, VA, 2014).
- <sup>40</sup>L. L. Su and B. A. Jorns, *J. Appl. Phys.* **130**, 163306 (2021).
- <sup>41</sup>S. E. Cusson, R. R. Hofer, R. B. Lobbia, B. A. Jorns, and A. D. Gallimore, in *35th International Electric Propulsion Conference, Atlanta, GA* (Electric Rocket Propulsion Society, 2017).
- <sup>42</sup>L. L. Su, A. R. Vazsonyi, and B. Jorns, in *AIAA Propulsion and Energy 2020 Forum* (American Institute of Aeronautics and Astronautics, Reston, VA, 2020).
- <sup>43</sup>L. L. Su and B. Jorns, in *AIAA Propulsion and Energy 2021 Forum* (American Institute of Aeronautics and Astronautics, Reston, VA, 2021).
- <sup>44</sup>L. L. Su, P. J. Roberts, T. Gill, W. Hurley, T. A. Marks, C. L. Sercel, M. Allen, C. B. Whittaker, M. Byrne, Z. Brown, E. Vigés, and B. Jorns, in *AIAA Scitech 2023 Forum* (American Institute of Aeronautics and Astronautics, Reston, VA, 2023).

- <sup>45</sup>J. L. Suazo Betancourt, “Laser Thomson scattering measurements of the plasma structure in the front pole region of a magnetically-shielded Hall effect thruster,” Ph.D. thesis (Georgia Institute of Technology, Atlanta, 2024).
- <sup>46</sup>J. Simmonds, R. R. Hofer, and M. L. R. Walker, “Personal communication of the H9v2 200G Magnetic Field Map between High-Power Electric Propulsion Laboratory Director and Electric Propulsion Group at NASA Jet Propulsion Laboratory” (2022).
- <sup>47</sup>R. A. Martinez, H. Dao, and M. L. R. Walker, *J. Propul. Power* **30**, 209 (2014).
- <sup>48</sup>D. A. Long, in *The Raman Effect: A Unified Treatment of the Theory of Raman Scattering by Molecules* (Wiley, 2002), pp. 31–48.
- <sup>49</sup>N. John and S. George, in *Spectroscopic Methods for Nanomaterials Characterization* (Elsevier, 2017), pp. 95–127.
- <sup>50</sup>J. L. Suazo Betancourt, S. J. Grauer, J. Bak, A. M. Steinberg, and M. L. R. Walker, *Rev. Sci. Instrum.* **95**, 043004 (2024).
- <sup>51</sup>M. J. van de Sande, “Laser scattering on low-temperature plasmas: High resolution and stray light rejection,” Ph.D. thesis (Eindhoven Technical University, 2004).
- <sup>52</sup>B. Vincent, “Incoherent Thomson scattering investigations in Hall thruster, planar magnetron and ECR ion source plasmas,” Ph.D. thesis (ICARE—Institut de Combustion, Aérothermique, Réactivité et Environnement, Orleans, 2019).
- <sup>53</sup>D. H. Froula, S. H. Glenzer, N. C. Luhmann, and J. Sheffield, in *Plasma Scattering of Electromagnetic Radiation* (Elsevier, 2011), pp. 31–44.
- <sup>54</sup>W. G. Vincenti, C. H. Kruger, and T. Teichmann, *Introduction to Physical Gas Dynamics - Hardcover* (Krieger Pub Co, 1975), ISBN 10: 0882753096, ISBN 13: 9780882753096.
- <sup>55</sup>H. Sugai, I. Ghanashev, M. Hosokawa, K. Mizuno, K. Nakamura, H. Toyoda, and K. Yamauchi, *Plasma Sources Sci. Technol.* **10**, 378 (2001).
- <sup>56</sup>S. F. Adams, J. A. Miles, and V. I. Demidov, *Phys. Plasmas* **24**, 053508 (2017).
- <sup>57</sup>A. A. Haji Abolhassani and J.-P. Matte, *Phys. Plasmas* **19**, 102103 (2012).
- <sup>58</sup>H. Amemiya, *J. Phys. Soc. Jpn.* **66**, 1335 (1997).
- <sup>59</sup>J. Lopez-Uricoechea, J. L. Suazo Betancourt, N. Butler-Craig, and M. L. R. Walker, “Spatially resolved Thomson scattering measurements of electron properties across the acceleration region of a high-power magnetically shielded Hall effect thruster,” *J. Appl. Phys.* (to be published).
- <sup>60</sup>B. Vincent, S. Tsikata, and S. Mazouffre, *Plasma Sources Sci. Technol.* **29**, 35015 (2020).
- <sup>61</sup>J. M. Haas and A. D. Gallimore, *Phys. Plasmas* **8**, 652 (2001).
- <sup>62</sup>J. M. Haas, “Low-perturbation interrogation of the internal and near-field plasma structure of a Hall thruster using a high speed probe positioning system,” Ph.D. thesis (University of Michigan, Ann Arbor, 2001).
- <sup>63</sup>R. R. Hofer, “Pepl,” Ph.D. thesis (University of Michigan, Ann Arbor, 2004).
- <sup>64</sup>P. J. Ryan, J. W. Bradley, and M. D. Bowden, *Phys. Plasmas* **26**, 040702 (2019).
- <sup>65</sup>T. J. Marks, B. A. Jorns, and M. L. R. Walker, “Personal communication of the Hall2De simulations of the H9 operating at the nominal 4.5 kW condition between High-Power Electric Propulsion Laboratory Director and Plasmadynamics and Electric Propulsion Laboratory Director” (2022).
- <sup>66</sup>B. Vincent, S. Tsikata, S. Mazouffre, and C. Boniface, in *36th International Electric Propulsion Conference University of Vienna Austria* (Electric Rocket Propulsion Society, 2019), <https://electricrocket.org/2019/384.pdf>
- <sup>67</sup>I. G. Mikellides, A. L. Ortega, I. Katz, and B. A. Jorns, in *52nd AIAA/SAE/ASEE Joint Propulsion Conference, 2016* (AIAA, 2016).
- <sup>68</sup>V. H. Chaplin, B. A. Jorns, A. Lopez Ortega, I. G. Mikellides, R. W. Conversano, R. B. Lobbia, and R. R. Hofer, *J. Appl. Phys.* **124**, 183302 (2018).
- <sup>69</sup>J. L. Suazo Betancourt, J. Lopez-Uricoechea, N. Butler-Craig, A. M. Steinberg, and M. L. R. Walker, *Rev. Sci. Instrum.* **95**, 043001 (2024).
- <sup>70</sup>P. J. Roberts, M. G. Allen, D. G. Brick, and B. A. Jorns, in *38th International Electric Propulsion Conference* (Electric Rocket Society, Toulouse, 2024).
- <sup>71</sup>T. A. Marks and B. A. Jorns, *J. Appl. Phys.* **134**, 153301 (2023).
- <sup>72</sup>I. G. Mikellides, I. Katz, R. R. Hofer, and D. M. Goebel, “Hall-effect thruster simulations with 2-D electron transport and hydrodynamic ions” (Jet Propulsion Laboratory, California Institute of Technology, Pasadena, CA, 2009), available at <http://richard.hofer.com/pdf/iepc-2009-114.pdf>
- <sup>73</sup>J. L. Suazo Betancourt, J. Lopez-Uricoechea, N. Butler-Craig, M. L. R. Walker, and A. M. Steinberg, “Laser Thomson scattering measurements indicate non-isothermal magnetic field lines in magnetically-shielded hall effect thrusters,” *Phys. Plasmas* (to be published).
- <sup>74</sup>M. J. Sekerak, R. R. Hofer, J. E. Polk, B. A. Jorns, and I. G. Mikellides, in *34th International Electric Propulsion Conference, Kobe* (Electric Rocket Propulsion Society, 2015), [https://electricrocket.org/IEPC/IEPC-2015-155\\_ISTS-2015-b-155.pdf](https://electricrocket.org/IEPC/IEPC-2015-155_ISTS-2015-b-155.pdf)